Nanoscale

PAPER

View Article Online
View Journal | View Issue

Cite this: *Nanoscale*, 2023, **15**, 11915

Exhaustive classification and systematic free-energy profile study of single-stranded DNA inter-overhang migration†

Hon Lin Too[a,b] and Zhisong Wang *[a,b]

Received 7th March 2023,
Accepted 16th June 2023

DOI: 10.1039/d3nr01058a

rsc.li/nanoscale

Migration of a short single-stranded DNA (ssDNA) between DNA overhangs is a basic molecular process that is widely used in dynamic DNA nanotechnology. The migration rate is sensitive to migration gaits, and limits the speed of dynamic DNA systems like DNA nanowalkers and other functional devices. Here, we identify and exhaustively classify all possible inter-overhang migration gaits of a ssDNA into only four categories based on their intrinsic symmetry. Using the oxDNA package, we conduct a systematic computational study for a typical migrator-overhang system to identify the lowest-energy pathway for all four migration categories. The one-dimensional free-energy profile along this pathway allows a parameter-free estimation of migration rates for all the four categories by the first passage time theory plus benchmarking from experimental rates available for one migration category. The obtained rates indicate a big room to improve DNA nanowalkers' speed above 1 μm per minute. The free-energy profile for each migration category possesses distinct and robust symmetric patterns, which largely decide local barriers, trapping states, and thereby a migration's rate-limiting processes and capacity for directional bias. This study thus provides a unified symmetry-based framework to analyze and optimize ssDNA migrations in kinetics, bias capacity, and structural design for better dynamic DNA nanotechnology.

1 Introduction

Migration of a short single-stranded DNA (ssDNA) on an array of DNA overhangs is a basic molecular process that is widely used in dynamic DNA nanotechnology. Such a minimal ssDNA migrator automatically displaces itself between two nearby single-stranded DNA overhangs (often called footholds) due to their dynamic competition to hybridize with the migrator. This automatic inter-overhang mobility has become a key element of numerous dynamic DNA nanosystems, especially DNA molecular motors.[1] Placed on an array of overhang footholds, a ssDNA migrator readily becomes a molecular walker that, despite no energy input, can move back and forth randomly along the overhang track. Long-range translocation far beyond nearby overhangs has been demonstrated for such energy-free and directionless ssDNA molecular walkers.[2,3] The ssDNA migrators have also been converted into directional molecular walkers[4,5] when an energy supply is supplied to cut the overhang footholds upon the migrator-foothold hybridization. This leads to so-called bridge-burning DNA walkers as the cutting triggers a downhill migration to a nearby intact foothold to give the walker a unique direction, but all the footholds will be successively damaged to lose the track function. The ssDNA migrators continue to be a crucial component for advanced non-bridge-burning DNA molecular walkers fully qualified as molecular motors, which are often double-stranded bipeds with two ssDNA migrators as legs. Either ssDNA migrator still does automatic migration between two adjacent overhangs which combine to form a composite binding site, and the inter-overhang migration is amplified into the bipedal walker's long-range directional translocation along a linear array of composite sites.

Following the schematic illustrations in Fig. 1a, a ssDNA migrator typically consists of three segments – a head toehold, a heel toehold, and an intermediate linker. A toehold is classified based on its relative distance to the track – the heel toehold is closer to the track compared to the head toehold. The gait is categorized based on the position change of migrator's exposed toehold that starts a forward migration from one overhang to another. For a ssDNA migrator, there are only two possible starting states – a heel starting state and a

[a]*NUS Graduate School for Integrative Science and Engineering, National University of Singapore, Singapore 117542. E-mail: phywangz@nus.edu.sg*
[b]*Department of Physics, National University of Singapore, 2 Science Drive 3, Singapore 117542*

† Electronic supplementary information (ESI) available: Additional discussion on the iterative reweighting umbrella sampling method and the minimum path sum used in this study, Migrator-track sequence and supporting figures Fig. S1–S9. See DOI: https://doi.org/10.1039/d3nr01058a

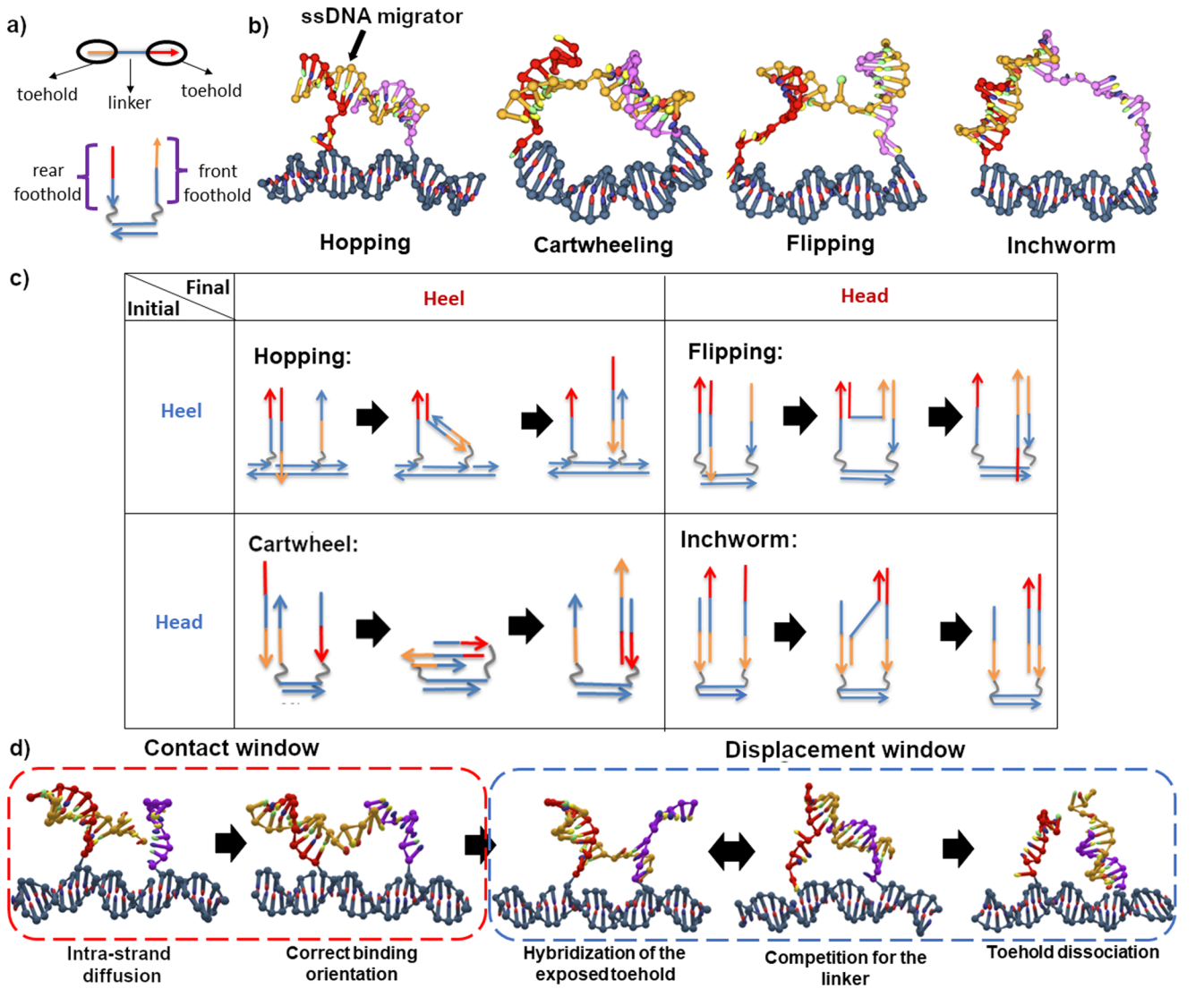

Fig. 1 Schematic of ssDNA migrators and their inter-overhang migration gait. (a) Components of a ssDNA migrator. The track and migrator are color coded such that the domains with the same color are designed to hybridize. The double-stranded segment of the track is 10bp and 20bp long, each colored segment is 5nt long. (b) The intermediate structure of all four inter-overhang migration gaits. The ssDNA migrator is colored orange, the track is colored dark blue, the front and rear footholds are colored purple and red respectively. (c) The inter-overhang migration gaits classification. There are only 2 possible starting states for this class of migrator – a heel starting state and a head starting state. After a successful migration, the exposed toehold either binds to the foothold domain that is close to the track (the heel configuration) or the domain that is far away from the track (the head configuration). (d) Process-based breakdown of migration. A complete migration starts with intra-strand diffusion of the exposed toehold, its hybridization to the front foothold, competition between the footholds for the linker, and toehold dissociation from the rear foothold.

head starting state. In the heel starting state, the heel toehold is exposed; while in the head starting state, the head toehold is exposed. After a successful migration, the exposed toehold binds to the second overhang at a foothold domain near the track and becomes a heel toehold (the heel state) or at the foothold domain far away from the track to become a head toehold (the head state). Thus, all imaginable inter-overhang ssDNA migrations can be classified into only four migration gaits, namely hopping (heel to heel), flipping (heel to head), cartwheeling (head to heel) and inchworm (head to head), as summarized in Fig. 1b and c. This classification is exhaustive as the backward reverse of the four migration types recovers either each other (*e.g.* hopping → inchworm) or itself (*e.g.* flipping and cartwheeling).

The flipping migration is used in light-powered DNA bipedal motors (with the migrator's heel[6] or head[7,8] segment linking the motor's intermediate duplex bridge). The hopping migration is used in an autonomous chemically fueled motor[9,10] and is later adapted into a light-powered motor.[11] The inchworm migration is used in bridge-burning DNA walkers[4,5] and many later variations[12–14] and applications.[15–17] The cartwheeling migration is used for a directionless DNA walker[3] that uses this single type of migration for long-range translocation along an overhang track on a DNA origami

platform. Another directionless DNA walker[2] combined the inchworm and hopping migration to achieve long-range translocation and thereby a robotic cargo-sorting task on a DNA origami platform.

Considering the wide application of inter-overhang ssDNA migration in dynamic DNA nanotechnology, understanding this basic process becomes important. The migration gait is often the most crucial rate-limiting factor for DNA walkers and other dynamic DNA nanosystems because the local binding geometry of DNA directly affects the diffusion rate, hybridization rate, dissociation rate and the chemical fuel invasion rate.[3,7,9,18–21] Therefore, an exhaustive study on all possible migration gaits is necessary to rationally design and optimize the migrator's performance. Computer simulation may be the most pragmatic approach to exhaustively study the inter-overhang migration due to its ability to identify structural change that may not be easily detected by experiments. The oxDNA simulation package,[22,23] an effective computational package based on a coarse-grained DNA model, has been widely used to study non-equilibrium processes such as the hybridization of DNA,[24,25] the walking of a bipedal DNA walker[9,26–28] and a burning bridge motor.[29] The basic physical properties of the ssDNA and dsDNA have been extensively studied by oxDNA, with the predicted radius of gyration[30] and persistence length[22,31,32] consistent with experimental data and all-atom simulations. The free-energy profile of different migration gaits as a function of design and operation parameters such as nucleotide sequences, inter-foothold distance, temperature and salt concentration[9,26–28] are easily obtainable from the simulation. The free-energy profile can be used to infer reaction pathways, estimate the migration rate for each gait, and study how each design and operation parameter affects the rate.

In this study, we report a systematic oxDNA computational study for the four migration categories, which exhaustively cover all possible inter-overhang ssDNA migration in broad dynamic DNA nanotechnology. The free-energy profile of each migration is extracted through the umbrella sampling method and the lowest energy pathway is studied. The inter-overhang migration rate is estimated from the first passage theory of a diffusion-controlled reaction.[33] Overall, we found that the migration gait affects the inter-overhang migration rate differently. Strategies to optimize the inter-overhang migration rate should therefore consider the migration gait.

2 Methodology

2.1 Simulation method

All simulations were run on oxDNA2 [31] force field, sequence-averaged interaction at 24 °C and 0.1 M [Na^+] salt concentration. oxview[34] was used for initial structure design, generation and visualization. Virtual Move Monte Carlo (VMMC)[35] was employed to sample the states visited by the system. To overcome the large transition barrier, the free-energy profile is extracted through the umbrella sampling method.[36] The iterative reweighting method is employed to ensure the data is well-sampled. More details on the simulation method can be found in the ESI.†

To sample the geometrical configuration of specific intermediate states, a few molecular dynamics (MD) simulations were performed on the oxDNA public server.[37] A mutual trap force field is introduced to all the binding nucleotides to ensure the system stays in the state of interest. All MD simulations were conducted in NVT ensemble, with a time step of dt = 3.03 fs for at least 5×10^8 simulation steps.

The schematic of the studied migrators is presented in Fig. 1a. The nucleotide sequences used are presented in Fig. S2 and S3.† The migrator is 15 nucleotides (nt) long and is divided into 3 equally long segments. Its performance is studied on 2 different tracks – a 10 base pair (bp) long and a 20bp long dsDNA track. Here, the track length refers to the inter-foothold distance (either 10bp or 20bp). A track can be designed to be either isoenergetic or downhill. An isoenergetic track consists of equally long front and rear footholds (10nt). On the other hand, a downhill track has an asymmetric foothold length. Since the ssDNA migrator prefers to be fully bound, the asymmetry creates an energetically favorable environment for forward migration, hence the name downhill. In this study, the inchworm migrator is the only migrator operating on a downhill track (15nt front foothold, 10nt rear foothold).

Process-wise, a successful migration starts from the intra-strand diffusion of the exposed toehold at the rear foothold, followed by the hybridization of the toehold to the front foothold, the competition between both footholds for the linker, and finally the dissociation of toehold from the rear foothold (see Fig. 1d). To effectively study these processes, the simulation is broken down into two windows – the contact window and the displacement window. The reaction coordinate in the contact window is the contact distance x between the toehold's tip and the front foothold. The free-energy in this window is defined as

$$G(x) = -k_B T \ln(p(x)) \quad (1)$$

where x is the contact distance and $p(x)$ is the normalised probability of x, *i.e.* $\int_x p(x)\mathrm{d}x = 1$.

Here, we assume that the toehold hybridizes with the foothold when x_{min} = 1.7 nm since this distance is smaller than the natural binding distance between a pair of nucleotides, which is 2.0 nm. The relative free-energy with respect to the reference state $\Delta G(x)$ is obtained from the following formula

$$\frac{\Delta G(x)}{k_B T} = -\ln\left(\frac{N(x)}{N_r}\right) \quad (2)$$

where $N(x)$ is the unbiased frequency of x, and N_r is the unbiased frequency of the reference state r. We chose r = x_{min} as the reference state. Then, the minimum free-energy required to initiate first contact is ΔG_{fc}

$$\Delta G_{fc} = -\Delta G_{min} \quad (3)$$

where ΔG_{min} is the minimum relative free-energy in the contact window.

The displacement window captures the hybridization process after a contact is formed. Its reaction coordinate is defined by two parameters – the total number of migrator's nucleotide bound to the rear foothold n_r and the total number of migrator's nucleotide bound to the front foothold n_f. The free-energy $G(n_f, n_r)$ is defined as

$$G(n_f, n_r) = -k_B T \ln(p(n_f, n_r)) \quad (4)$$

where $p(n_f, n_r)$ is the normalised probability of finding the system in state (n_f, n_r), *i.e.* $\sum_{n_f, n_r} p(n_f, n_r) = 1$. The relative free-energy with respect to the reference state $\Delta G(n_f, n_r)$ is obtained from the following formula

$$\frac{\Delta G(n_f, n_r)}{k_B T} = -\ln\left(\frac{N(n_f, n_r)}{N_r}\right) \quad (5)$$

where $N(n_f, n_r)$ is the unbiased frequency of state (n_f, n_r), and N_r is the unbiased frequency of the reference state r. We chose the most frequently visited state as the reference state.

In this window, a migrator starts from the initial state $(n_f, n_r) = (1, 10)$ and ends at (10, 1) (or (14, 1) for the downhill track). Therefore, to obtain the 1D lowest energy pathway, we search for the minimum path sum in the 2D free-energy landscape. The minimum path sum for each gait is highlighted in Fig. 3a–d and Fig. S6–S9.† We refer the readers to the ESI† for more details on the method to obtain the minimum path sum.

2.2 Bending angle between neighboring nucleotides

In the oxDNA model, a DNA is treated as a string of rigid nucleotides. The position and orientation of each nucleotide are described by 3 vectors – a center of mass vector, a backbone-nucleobase vector $\vec{b}_i$, and a normal vector that is perpendicular to the nucleotide's plane. In this work, the bending angle between neighboring nucleotides $\theta_{i,i+1}$ is defined as the angle between their backbone-base vectors (see Fig. S5a†).

$$\cos\ \theta_{i,i+1} = \frac{\vec{b}_i \cdot \vec{b}_{i+1}}{\| \vec{b}_i \| \cdot \| \vec{b}_{i+1} \|} \quad (6)$$

Since the DNA is a helix structure, the natural bending angle between a pair of neighboring nucleotides is around 36°. In this study, a strong bending occurs when the average bending angle between any nucleotide pair is larger or equal to 90°, *i.e.* $\langle \theta_{i,i+1} \rangle \geq 90°$.

2.3 Reaction rate calculation

The contact rate $k_{contact}$ is the inverse of average time taken for a migrator to reach x_{min}. According to the first passage time theory by Szabo *et al.*,[33] the contact rate can be approximated as:

$$k_{contact}^{-1} = \int_{x_{min}}^{\infty} dx D_1^{-1} p(x)^{-1} \left[\int_x^{\infty} dy p(y)\right]^2 \quad (7)$$

where D_1 is the diffusion coefficient in the contact window.

The displacement rate $k_{displace}$ is the inverse of average time for a migrator to displace from the rear foothold to the front foothold on the lowest energy pathway immediately after first contact. Since the reaction coordinate is discrete, the displacement rate can be approximated as

$$k_{displace}^{-1} \approx \sum_{i=0}^{n} D_2^{-1} p(i)^{-1} \left[\sum_{j=i}^{n} p(j)\right]^2 \quad (8)$$

where D_2 is the diffusion coefficient in the displacement window, i is the state in 1D lowest energy pathway, and n is the total number of states in the lowest energy pathway. The reaction occurs when the system is in the state $i = 0$. States are indexed with non-negative integers as shown in Fig. 3e and f.

3 Results and discussion

3.1 Free-energy profile analysis for all migration gaits

We first considered the free-energy profile in the contact window. Fig. 2a shows the free-energy of 4 different gaits as a function of contact distance x on a 10bp track. The first-contact free-energy ΔG_{fc} increases in the order of hopping ≈ flipping < downhill inchworm < cartwheeling. Overall, a gait with an exposed heel toehold requires a lower first-contact free-energy compared to those with an exposed head toehold. This is because the exposed head toehold has a rigid duplex beneath that keeps it away from the front foothold (see Fig. 2b *vs.* c).

The hopping gait has a significantly lower ΔG_{fc} than its counterpart, inchworm, due to the difference in their starting states. This asymmetry means a hopping migrator requires a larger energetic cost to backward migrate after a successful forward migration since it is harder for the inchworm gait to form contact. The difference in energetic cost provides a natural directional bias to the hopping gait as far as the first contact is concerned. On the other hand, gaits which are the backward reverse of themselves (cartwheel and flip) have no such bias.

Fig. 3a–d show the displacement free-energy landscapes on a 10bp track. In general, the minimum is located at the state where the migrator is fully bound to both footholds (*i.e.* $n_f + n_r = 15$). The 1D lowest-energy pathways in Fig. 3e and f elucidate some common features for all migration gaits. Firstly, the 5 consecutive transitions from the (1,10) state to the (5,10) state is normally a downhill process. This corresponds to the zippering of exposed toehold to the front foothold. Secondly, if the track is isoenergetic, the free-energy of the initial and final states is similar. Thirdly, for all isoenergetic tracks, there is an inevitable uphill curve near the end of inter-overhang migration. This energy barrier corresponds to the energetic cost to dissociate the toehold from the rear foothold.

The biggest difference between the gaits lies in the competition phase – where the front and rear footholds compete for the migrator's linker. This phase largely determines if the lowest-energy profile is symmetrical. In this phase, the free-energy can form a flat plateau or a sharp energy well. The toehold mediated strand displacement (TMSD) mechanism in

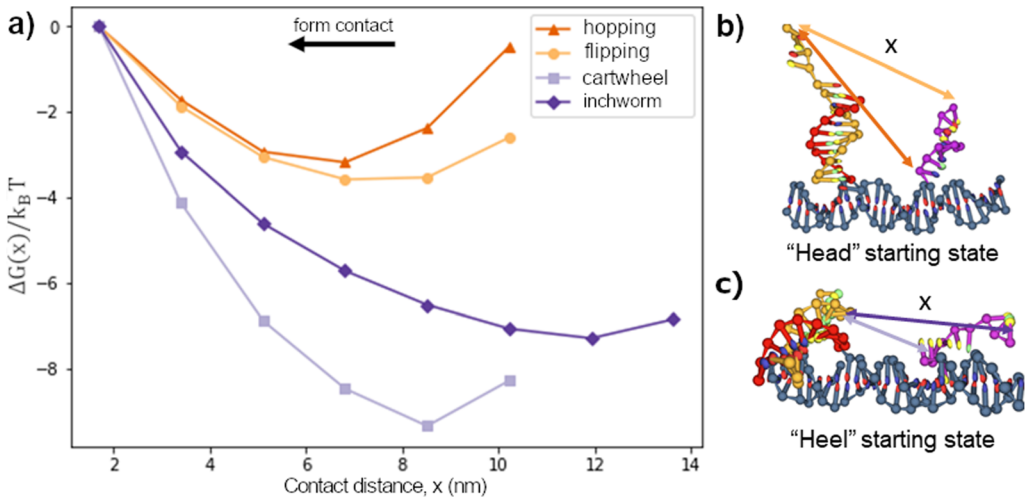

Fig. 2 (a) The contact free-energy of a 15nt long ssDNA migrator on a 10bp track and (b and c) its typical starting configurations. The arrows in (b and c) are color-coded to show each gait's contact distance x to form contact. Migrators in the head starting state (cartwheel and downhill inchworm) are normally perpendicular to the track, whereas migrators in the heel starting state (flip and hop) are normally parallel to the track.

a cartwheel migrator flattens the free-energy during the competition process,[19,38] which is observed on a 20bp track (see Fig. 4g). The flat plateau makes the free-energy profile highly symmetrical. However, on a short 10bp track, this symmetry is broken. This is because the track-migrator binding induces a strong internal tension, which forces the migrator to bend (see Fig. S4†). This bending increases the difficulty for the front foothold to invade the linker. Therefore instead of a flat plateau, an energy well is observed.

The flipping migrator's free-energy profile is highly symmetrical due to the flat plateau in the competition phase. The symmetry comes from the unique "U"-shaped configuration when the migrator is fully bound to both footholds (see Fig. S5a†). The "U"-shaped configuration induces a strong bending on the migrator. To verify this, we plotted the 2D bending angle histogram in (8,7) and (10,5) states. Both plots show there is at least a nucleotide pair with a mean bending angle greater than 90°. Similar strong bending is unavoidable in (8,7), (10,5) and other fully bound states, thus the symmetrical free-energy profile.

On the other hand, a hopping migrator contains a sharp minimum at the (10,5) state. The sharp minimum located near the end of the lowest-energy pathway breaks the symmetry of its free-energy profile. To understand this, we analyzed the migrator bending angle distribution of the (5,10) and (10,5) state. From Fig. S5e and f,† the (5,10) state contains a nucleotide pair with strong bending (larger than 125°), but this geometrical feature is not found in the (10,5) state. The absence of strong bending in the (10,5) state is energetically favored, hence the formation of a sharp minimum. The sharp minimum indicates that a hopping migrator contains a well-defined intermediate structure. This feature may be useful for structure-based selective control of migration.

Since the inchworm gait is the backward reverse of the hopping gait, the inchworm free-energy profile is the mirror image of its counterpart. On a downhill track, the inchworm free-energy profile contains a sharp minimum located at the (5,10) state and is immediately followed by an energy barrier before completely dissociating from the rear foothold. Again, the bending angle distribution of the migrator is plotted (see Fig. S5h†). For the (5,10) state, 30°–40° is the most common bending angle across all nucleotide pairs, indicating the lack of strong bending. This makes the (5,10) state the energetically most favorable state. The fully bound intermediate states after the (5,10) state show a clear sign of strong bending (see Fig. S5i† for (9,6) state), which is energetically unfavorable. Such energetic difference at the beginning and middle of the reaction pathway breaks the symmetry in its free-energy profile.

3.2 Migrator optimization strategy differs from gait to gait

Since the free-energy profile is sensitive towards the local geometry, the energy profile can be tuned by changing the inter-foothold distance, migrator length or introducing spacers between the footholds and track. The goal of this section is to understand how these design parameters affect the free-energy profile. Here, we fixed the migrator's length and focused on the effect of inter-foothold distance and spacer.

Fig. 4a–d show the free-energy profile in the contact window. In general, the larger the inter-foothold distance, the larger the free-energy ΔG_{fc} to form first contact. Hopping is the only gait that could not initiate first contact when the inter-foothold distance increases to 20bp. This gait has the shortest reach, which is why in the cargo sorting robot, the rear foothold is designed to have unusually long rear spacers (11nt long) to ensure the first contact can be initiated when it conforms to the hopping gait.[2]

The rear spacers are more effective in decreasing ΔG_{fc} of both cartwheel and inchworm migrators compared to the front foothold. To initiate first contact, the head starting migrators bend the joint between the rear foothold and the track. They

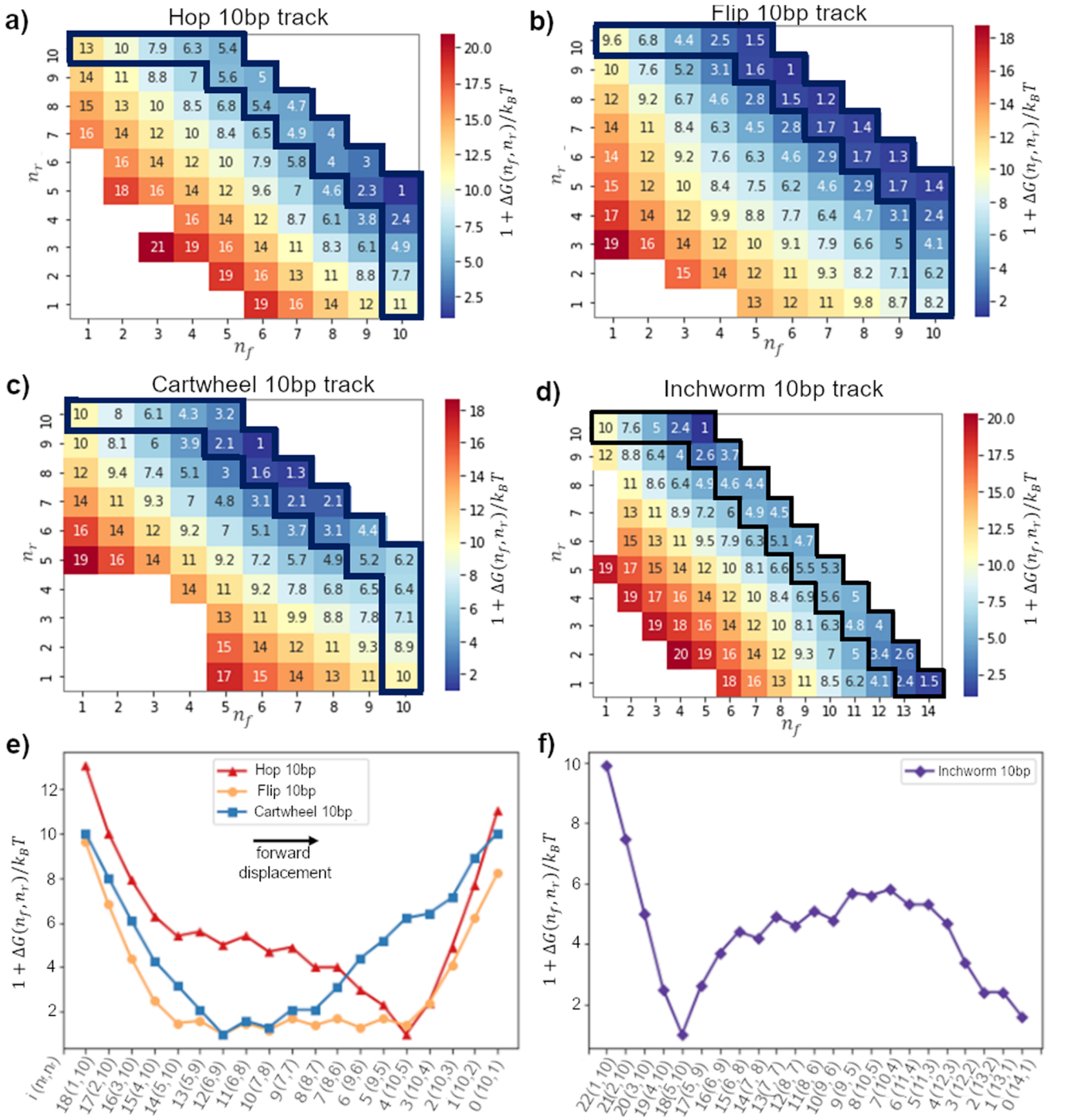

Fig. 3 (a)–(d) The 2D free-energy landscape of 4 different gaits on a 10bp track. The relative free-energy is shifted upward by $1k_BT$. A successful forward displacement starts from the (1,10) state (upper left) and ends at the (10,1) state or (14,1) state (lower right). The black box shows the minimum path sum for each gait. (e) and (f) The 1D lowest-energy reaction pathway extracted from their respective 2D free-energy profile. The *x*-axis shows the state (n_f, n_r) and its index *i*.

suffer from a larger energetic penalty to initiate first contact. Therefore, the conformation flexibility provided by the rear spacers will be more effective in reducing ΔG_{fc}. On the other hand, both flipping and hopping migrators do not bend as much as they are already parallel to the track. Therefore, their ΔG_{fc} are not sensitive towards the spacers location.

The displacement window's free-energy landscape is also sensitive to the local geometry. Fig. 4e–h show the 1D lowest-energy reaction pathway of all 4 gaits on different tracks. In general, a longer inter-foothold distance decreases the energy to dissociate the toehold from the rear foothold. The reduction is probably contributed by the larger internal tension on a longer track. However,

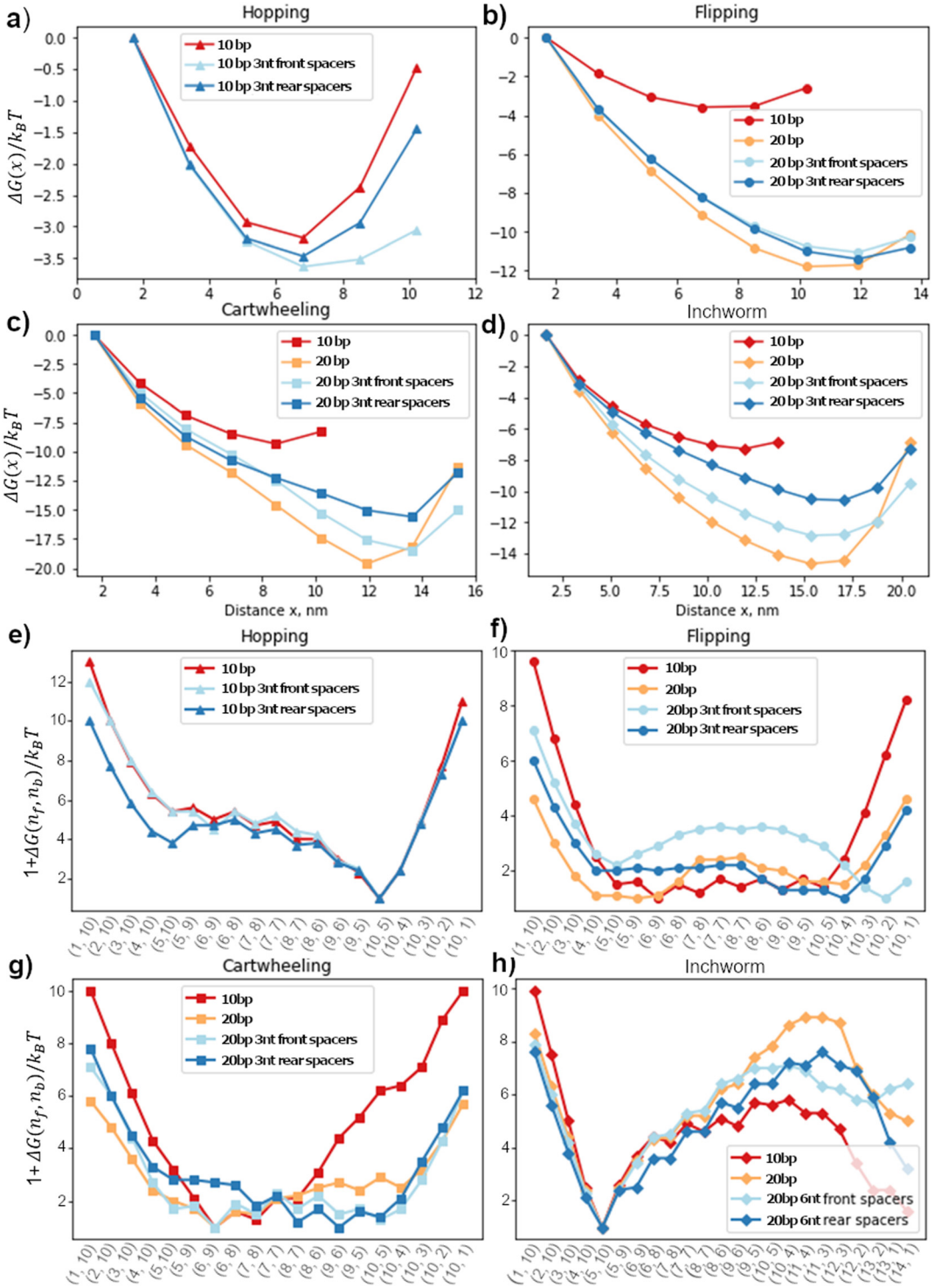

Fig. 4 Free-energy profile of migrators on different track and windows. (a)–(d) The contact free-energy on different tracks. The track is spacer less unless stated otherwise. (e)–(h) The 1D lowest-energy reaction pathway for all gaits on different tracks.

for a downhill inchworm migrator, its dissociation energy increases significantly on a longer track. This energy barrier can be reduced by introducing spacers to the track (Fig. 4h). We found that the 6nt front spacers track is more effective in lowering the energy barrier than the track with 6nt rear spacers.

The free-energy profile of a cartwheeling migrator during its competition phase is flatter on a longer inter-overhang distance. This is consistent with the TMSD free-energy profile without any geometrical constraint[38] because the TMSD is more efficient when the migrator's linker is straight to ease the front foothold

invasion. The flat free-energy profile on a 20bp track in the competition phase, followed by a sharp increase in the dissociation phase is also consistent with the experiment by Li *et al.*[3] They found that the transition rate between the intermediate states in the competition phase are high, but the dissociation rate from the rear foothold is significantly lower and is therefore the rate-limiting process of this migration gait.

3.3 Rate estimation

The computed free-energy profiles in Fig. 4 allow the estimation of migration rates *via* the first-passage time theory (Methods). However, the contact window and the displacement window have different effective diffusion coefficients (D_1 and D_2 in eqn (7) and (8)) that are not well determined from experiments. The contact rate depends on the intra-chain diffusion coefficient for the ssDNA migrator, *i.e.*, D_1 in eqn (7). For such intra-nucleotide diffusion, a measured coefficient of D_1–1.4×10^4 nm^2 s^{-1} is reported in ref. 39. Table 1 gives the contact rate for the four types of migrations estimated using this measured D_1 value and the free-energy profiles in Fig. 4a–d. The displacement rate depends on the effective diffusion coefficient of the hybridization, strand displacement and strand dissociation, *i.e.*, D_2 in eqn (7), which is largely unknown. The contact rate and displacement rate combine to determine the total migration rate, which is ~0.04 s^{-1} as reported from a recent single-molecule study by Li *et al.*[3] for an 18nt-long migrator cartwheeling migrator over 20bp inter-overhang gap. Exploiting this measured rate for a common benchmark, we can have a reasonably reliable rate estimation for all four migration types as follows.

We first carry out the same oxDNA simulation for the measured cartwheeling migration (18nt migrator over 20bp inter-overhang gap) to obtain its free-energy profiles for the contact window and for the energy-minimum pathway for the displacement window (Fig. 5). Then we apply the same first-passage time formula (eqn (7) and (8)) to the free-energy profiles, yield the rates for the two windows as the function of diffusion coefficients D_1 and D_2. By a crude but reasonable approximation, the two diffusion coefficients may be assumed to be independent of the migration gaits, inter-overhang distance and migrator length. As a consequence, the ratio of computed contact rates between any migration and the measured migration is independent of the uncertain diffusion coefficient D_1. Similarly, the ratio of computed displacement rates between any migration and the measured migration is independent of the uncertain diffusion coefficient D_2. The two rate ratios, which are given in Table 1, allow a parameter-free cross-migration rate comparison for each window on the same footing. Perhaps more importantly, the two rate ratios also allow quantitative estimation of the magnitude of total rates for all the migrations based on the benchmark of the experimentally measured cartwheeling rate.

Taking the rate ratios for the contact window and displacement window as $\gamma_1 = \frac{k_{15,\mathrm{contact}}}{k_{18,\mathrm{contact}}}$ and $\gamma_2 = \frac{k_{15,\mathrm{displace}}}{k_{18,\mathrm{displace}}}$, we have the total rates k_{15} and k_{18} satisfying $\frac{1}{k_{15}} = \frac{1}{k_{15,\mathrm{contact}}} + \frac{1}{k_{15,\mathrm{displace}}}$ and $\frac{1}{k_{18}} = \frac{1}{k_{18,\mathrm{contact}}} + \frac{1}{k_{18,\mathrm{displace}}}$ as a complete migration is the diffusive contact followed by displacement (Fig. 1d). Hence total rates for a 15nt migrator k_{15} and for the experimentally measured 18nt cartwheeling migrator k_{18} are

$$k_{15} = \frac{\gamma_1\gamma_2 k_{18,\mathrm{contact}} k_{18,\mathrm{displace}}}{\gamma_1 k_{18,\mathrm{contact}} + \gamma_2 k_{18,\mathrm{displace}}} \quad (9)$$

$$k_{18} = \frac{k_{18,\mathrm{contact}} k_{18,\mathrm{displace}}}{k_{18,\mathrm{contact}} + k_{18,\mathrm{displace}}} \quad (10)$$

yielding a ratio between the two total rates

$$\frac{k_{15}}{k_{18}} = \frac{\gamma_1\gamma_2(k_{18,\mathrm{contact}} + k_{18,\mathrm{displace}})}{\gamma_1 k_{18,\mathrm{contact}} + \gamma_2 k_{18,\mathrm{displace}}} \quad (11)$$

If $\gamma_1 > \gamma_2$, the ratio $\frac{k_{15}}{k_{18}}$ has a lower limit by replacing γ_2 in its denominator with γ_1 and a upper limit by replacing γ_1 in its denominator with γ_2, namely $\gamma_2 < \frac{k_{15}}{k_{18}} < \gamma_1$. Similarly, the ratio follows $\gamma_1 < \frac{k_{15}}{k_{18}} < \gamma_2$ if $\gamma_1 < \gamma_2$ and $\frac{k_{15}}{k_{18}} = \gamma_1$ if $\gamma_1 = \gamma_2$. Thus, the ratios in Table 1 yield the absolute rate over a certain range for all the migration based on the experimentally reported rate[3] of

Table 1 Table of normalized rate in both contact and displacement windows on different tracks. The third column k_{contact} is the contact rate calculated using the diffusion coefficient 1.4×10^4 nm^2 s^{-1} reported by Wallace *et al.*[39] The fourth column is the contact rate normalized to the 18nt cartwheeler's contact rate. The fifth column is the displacement rate normalized to the 18nt cartwheeler's displacement rate. Li *et al.* reported that the 18nt cartwheeler has a median migration time of 23.6 s, or a total rate of $k_{18} \sim 0.04$ s^{-1} (ref. 3)

Gait	Track	k_{contact} (nm^2 s^{-1})	$\frac{k_{15,\mathrm{contact}}}{k_{18,\mathrm{contact}}}$	$\frac{k_{15,\mathrm{displace}}}{k_{18,\mathrm{displace}}}$
Flip	10bp	2.5×10^2	2.5×10^4	9.0×10^0
	20bp	8×10^{-2}	1.0×10^1	2.0×10^2
	20bp 3nt front spacers	2×10^{-1}	2.3×10^1	2.0×10^3
	20bp 3nt rear spacers	1×10^{-1}	1.7×10^1	4.0×10^2
Cartwheel	10bp	2.3×10^0	1.8×10^2	3.0×10^0
	20bp	6×10^{-5}	8×10^{-3}	1.2×10^2
	20bp 3nt front spacers	2×10^{-4}	2×10^{-2}	7.2×10^1
	20bp 3nt rear spacers	3×10^{-3}	3×10^{-1}	8.0×10^1
	20bp Li *et al.* 18nt migrator[3]	7×10^{-3}	1	1
Downhill inchworm	10bp	8.3×10^0	7.5×10^2	1.4×10^2
	20bp	4×10^{-3}	5×10^{-1}	5.0×10^0
	20bp 6nt front spacers	2×10^{-2}	3.0×10^0	1.9×10^1
	20bp 6nt rear spacers	2×10^{-1}	2.5×10^1	1.7×10^1
Hop	10bp	3.7×10^2	4.3×10^4	3.0×10^0
	10bp 3nt front spacers	1.8×10^2	2.4×10^4	7.0×10^0
	10bp 3nt rear spacers	2.4×10^2	3.1×10^4	6.0×10^0

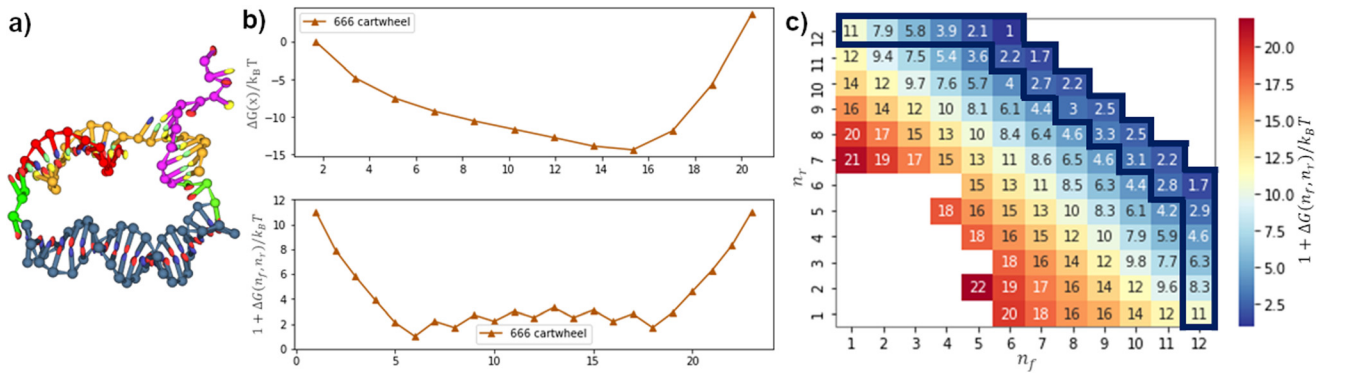

Fig. 5 (a) The 18nt long cartwheel migrator on a 20bp long track studied by Li *et al.* The track contains 3nt spacers at both the front and rear foothold (colored in green). (b) Its contact free-energy and 1D lowest-energy reaction pathway and (c) the 2D free-energy profile in the displacement window.

$k_{18} \sim 0.04\ s^{-1}$. Considering the 10bp inter-overhang gap, the resultant rates are $0.36\ s^{-1} < k_{15,flip} < 1.0 \times 10^3\ s^{-1}$ for the flipping, $0.12\ s^{-1} < k_{15,cw} < 7.2\ s^{-1}$ for the cartwheeling, $5.6\ s^{-1} < k_{15,inchworm} < 30\ s^{-1}$ for the downhill inchworm, and $0.12\ s^{-1} < k_{15,hop} < 1.7 \times 10^3\ s^{-1}$ for the hopping. These lower limits are a conservative but reliable experiment-informed estimate of practically accessible rates for the four types of migration over the same 10bp inter-overhang gap, *i.e.*, $0.36\ s^{-1}$ for the flipping, $0.12\ s^{-1}$ for the cartwheeling, $5.6\ s^{-1}$ for the downhill inchworm, and $0.12\ s^{-1}$ for the hopping.

3.4 Migration speed, and practically accessible speed of DNA nanowalkers

The lower limits obtained in this study for the total migration rates (Table 1, rightmost column) provide a reliable experiment-calibrated estimation of accessible speed for DNA walkers, including both ssDNA walkers and bipedal walkers. Considering again the 15nt migrator over the 10bp inter-overhang gap, the lower rate limits times the inter-overhang distance (~3.4 nm) yield the realistic migration speed for the four types of ssDNA migrators as ~73 nm min^{-1} for the flipping, 24 nm min^{-1} for the cartwheeling, $\sim 1.1 \times 10^3$ nm min^{-1} for the downhill inchworm, and ~24 nm min^{-1} for the hopping. These migration speed values, which are for a single inter-overhang migration step, offer directly a realistic upper bound for the speed of bridge-burning and directionless DNA nanowalkers as the two types of walkers are typically made of a ssDNA migrator with its on-track walking implemented by a single type of inter-overhang migration (now over a linear array of often equal-spaced overhangs). As for advanced track-walking bipedal DNA motors, their steps are typically completed by an energy-driven dissociation of the motor's rear leg from a two-legged motor-track binding state, followed by forward inter-overhang migration of the front leg within a bi-overhang site and the biased binding of the rear leg to a front site. Among the three molecular processes, the inter-overhang migration is often the rate-limiting process as the leg dissociation rate is readily promoted beyond the migration rate (*e.g.*, $0.12\ s^{-1}$–$5.6\ s^{-1}$ for the 15nt migrator over 10bp gap) by the externally controlled rate for energy supply (*e.g.*, high fuel concentration[40] or strong light irradiation[6]), and the forward leg binding rate also can reach[41] a high level of $10\ s^{-1}$–$100\ s^{-1}$ for small nanowalkers. Hence the above migration speed values also offer a conservative and realistic upper bound for the overall speed of advanced bipedal DNA motors, *i.e.*, from ~24 nm min^{-1} up to $\sim 1.1 \times 10^3$ nm min^{-1}.

The reported DNA nanowalkers are already near the low end of the above speed range (*i.e.*, ~24 nm min^{-1}) but still far away from the high end (*i.e.*, $\sim 1.1 \times 10^3$ nm min^{-1}). An autonomous chemically fueled DNA bipedal motor[9] adopting the hopping migration achieves a speed of ~8 nm min^{-1} as found by a recent single-molecule mechanical study[10] using magnetic tweezers. This motor speed is not far from the ~24 nm min^{-1} migration speed for the hopping. A bridge-burning ssDNA walker adopting the downhill inchworm migration reaches a speed of ~6 nm min^{-1} as found by a single-molecule imaging study[42] using atomic force microscopy. The latest autonomously chemically fueled DNA bipedal motor[43] based on the cartwheeling migration achieves ~30 nm min^{-1} speed. This goes beyond the conservative estimation of ~24 nm min^{-1} migration speed for cartwheeling likely because the motor adopts a downhill cartwheeling instead of the isoenergetic cartwheeling in this study. Overall, there exists a big room to further improve DNA nanowalkers up to the predicted speed of $\sim 1.1 \times 10^3$ nm min^{-1}, which is ~40 times lower than the speed of a fast archetypal biological molecular motor called kinesin[44] (~800 nm s^{-1}). Practical accessibility of the target speed of $\sim 1.1 \times 10^3$ nm min^{-1}, *i.e.*, ≲20 nm s^{-1}, is also supported by the single-molecule mechanical study for the hopping-based DNA bipedal motor. The single-motor trajectories from this study[10] show, though often with long inter-step pause, fast individual steps – sometimes less than 0.2 seconds per ~16 nm step. This experimental finding concurs with the present computational study for the conclusion that the DNA migration kinetics is fast enough to support DNA nanowalkers up to the speed of 1000 nm min^{-1}, especially for DNA motors with good directionality.

This study provides guidelines for accelerating inter-overhang migration for faster DNA nanowalkers. Adapting the four

types of isoenergetic migration into downhill migration can accelerate the migration non-trivially, as evidenced from the higher migration speed for the downhill inchworm migrator than the other three isoenergetic migrators. The parameter-free cross-migration comparison for the contact window or the displacement window reveals more mechanistic insights. When the inter-overhang gap widens from 10bp to 20bp for the flipping and cartwheeling migrators (all 15nt long), the contact rate decreases but the displacement increases as shown by the rates normalized to that of the common benchmarking 18nt migrator (*i.e.*, rate ratios $k_{15,\mathrm{contact}}/k_{18,\mathrm{contact}}$ and $k_{15,\mathrm{displace}}/k_{18,\mathrm{displace}}$ in Table 1). The trend is clear – a longer foothold distance increases the gap for the first contact to reduce the contact rate, but also increases the intra-migrator tension that helps to dissociate the migrator from the rear foothold (hence increasing the displacement rate). Thus, the speed optimization for the flipping and cartwheeling migration involves a trade-off between the contact window and the displacement window. For the downhill inchworm, both the contact rate and the displacement rate decrease with the widening inter-overhang gap. This may be attributed to the higher energy barrier for the 20bp inter-overhang gap than the 10bp gap for both the contact and displacement windows (Fig. 4d and h). Thus, a good strategy to accelerate this type of migration is to reduce the foothold distance.

3.5 From inter-overhang migration to directional bias of bipedal DNA nanowalkers

A bipedal DNA walker may have its two legs as two ssDNA migrators, often of the same type and with their heads or heels connecting to the intermediate duplex bridge of the bipedal walker. The two overhangs supporting the migrations in this study, if arranged repeatedly into a linear periodic array, form the track for the bipedal walker. If the walker has one leg binding to such a bi-overhang site and the other leg mobile above the track, the inter-site migration of the track-bound leg may place the other leg closer to the front site but further from the rear site, resulting in a directional bias (*i.e.*, preferential forward leg binding) for the bipedal walker. Such a bias, which amplifies[45,46] a small local displacement within a single binding site into long-range inter-site directional walking, has been found in biological bipedal molecular motors (*e.g.*, kinesin,[47] myosin V[48]) and also implemented in artificial DNA molecular motors[6–11,27,49,50] through the inter-overhang migrations on an *ad hoc* basis. This study now allows an exhaustive counting of all migration types capable of the bias. At first glance, all four types of migration provide the bias whether the ssDNA migrator's head or heel segment is linked to the other mobile leg of a bipedal walker since the average location of the migrator's head (or heel) is displaced forward over a distance equivalent of the inter-overhang gap d_0 (assuming, for sake of general discussion, the walker's direction always follows the forward direction of inter-overhang migrations shown in Fig. 1c).

However, the magnitude of this bias differs between the migration types, and is sensitive to their free-energy profiles, migrator-overhang binding structure, and the migrator's linkage to the other leg of a motor. The hopping migration, if fully completed as illustrated in Fig. 1c, provides a rather big and robust bias because the most forward location of the migrator's heel is also displaced forward by a distance $\sim d_0$, and the same is true for the migrator's head *via* back-and-forth swing of the migrator-overhang duplex after migration. Similar biases are provided by the inchworm migration due to virtually the same displacement for the most forward location of the migrator's head or heel. However, the hopping migration may be paused at the trapping state near the final stage (corresponding to the potential well in Fig. 4e), in which the migrator-overhang binding structure has the migrator's heel segment near the bottom of the front overhang but the head segment still bound with the first overhang and tilted backward (see Fig. 1b, leftmost plot; also consistent with an early study[51]). The trapping state retains the forward bias if the migrator's heal segment is linked to the other leg, but produces a slight backward bias if the head segment is linked to the other leg. This is consistent with an autonomous chemically fuelled DNA bipedal motor[8,9,27] (also a latter light-powered version[11]) that exploits the trapping state of the hopping migration (with the ssDNA migrator leg's head linked to the other migrator leg) and indeed shows a weak backward bias in absence of fuels (but overcome by a chemomechanical coupling effect[9,11] in presence of fuels). The inchworm migration has a trapping state too but near the early stage (corresponding to the potential well in Fig. 4h), with the migrator being bound with the first overhang almost entirely (see migrator-overhang binding structure in Fig. 2b, rightmost plot). Regardless of the inchworm migrator's linkage to the other leg, the trapping state largely delays the forward bias until the migration further proceeds for the migrator's full dissociation from the first overhang (*e.g.*, by downhill migration).

Compared to the hopping and cartwheeling migration, the flipping migration provides an even better bias if the ssDNA migrator's heel is linked to the other mobile leg, because the heel's most forward location is displaced by $\sim d_0$ plus the length of post-migration migrator-overhang duplex. The same migration provides a reduced bias if the migrator's head is linked to the other leg, because the migration-induced displacement for the head's most forward location is roughly equal to the length of pre-migration migrator-overhang duplex minus d_0. Similarly, the cartwheeling provides a reduced bias with the migrator's head linked to the other leg but a good bias with the heel linked to the other leg (near the best bias for the flipping). The flipping and cartwheeling migration have no well-defined trapping state due to their flat free-energy profiles (Fig. 4f and g, except for cartwheeling at small inter-overhang gap). Nevertheless, the best bias for the two types of migration is still delayed until the migrator's full dissociation from the first overhang. Fig. 1b shows the typical intermediate migrator-overhang binding structures that hold the migrator largely before the front overhang. This structural pattern is rather stable before the full migration although the migrator's base pairs with the two overhangs may change dynamically due to the flat free-energy profile (with the total number of

base pairs roughly fixed, see the horizontal axis for Fig. 4f and g). The flipping-based bias is consistent with the forward leg binding bias observed in two light-powered DNA bipedal motors, which use the flipping ssDNA legs with either heal-to-heel connection[6,49,50] or head-to-head connection[7,8,27] through the intermediate duplex.

As seen in Fig. 4e–h, the free-energy profile pertinent to directional biases is reversely asymmetric between the hopping and inchworm migration, but mostly flat and symmetric for the flipping and cartwheeling. These symmetric patterns are rather robust regardless of parameter changes (*e.g.* inter-overhang gap, spacers under overhangs, isoenergetic or downhill). These stable symmetric patterns in the free-energy profiles are largely decided by the intrinsic symmetry of the different migration gaits: the reverse of flipping or cartwheeling is itself but the reverse of hopping is inchworm and *vice versa*. These distinct and robust symmetric patterns of free-energy profiles largely decide intermediate states or trapping states and their structures, thus forming a conceptually clear basis for designing and analyzing biases and overall directionality[52–54] of advanced bipedal DNA motors. We note that the speed of a DNA nanowalker is determined not only by the DNA migration kinetics but also by the walker's overall directionality. As a consequence, a directional DNA walker has a higher speed than a directionless DNA walker even if both walkers possess the same level of DNA kinetics. Therefore, improving the speed of DNA nanowalkers requires not only faster DNA kinetics but also better biases and directionality. Furthermore, the distinct symmetric patterns of the one-dimensional free-energy profiles, which correspond to the lowest-energy pathways pertinent to the migration kinetics, also largely decide local barriers and rates. Hence the often complex task of rate optimization can be conveniently guided by modulating the symmetric patterns of the free-energy profiles along the lowest-energy pathways by adjusting design parameters. Altogether, this study provides a unified symmetry-based conceptual framework for computation-aided and sequence-dependent optimization of DNA migration kinetics and biases (*i.e.* through the chain of oxDNA computed two-dimensional free-energy landscape → identified lowest-energy pathway, the associated one-dimensional free-energy profile, and symmetry analysis → intermediate states, structures and barriers → rates and biases). This conceptual framework covers all possible ssDNA inter-overhang migrations, classified exhaustively into four categories that each possess distinct symmetries in gaits and in free-energies along the lowest-energy pathways.

4 Conclusions

In summary, all possible types of inter-overhang migration of ssDNA migrators, which play a key role in DNA nanowalkers and wider dynamic DNA nanotechnology, are exhaustively identified based on their intrinsic gait symmetry, and classified into only four categories. The free-energy landscape for all four migration categories is obtained from realistic sequence-dependent simulation for typical migrator-overhang systems. The free-energy landscape allows the lowest-energy migration pathway to be identified, yielding a one-dimensional free-energy profile along the pathway that is pertinent to the migration kinetics. Using an experimentally measured migration rate as a benchmark, a parameter-free estimation of migration rates is achieved for all four migration categories. The resultant rates are compatible with reported DNA nanowalkers and indicate a big room to further improve the present DNA nanowalkers – up to a speed above 1 μm per minute. This speed is practically accessible for DNA walkers, especially directional DNA bipedal nanomotors. This target speed is only ~40 times below the speed of the fastest biological molecular motor (kinesin), and suffices for many real-world nanotechnological applications. Besides, the free-energy profile along the lowest-energy migration pathway is found to possess distinct and robust symmetric patterns for the four migration categories due to their intrinsic gait symmetry. The symmetric patterns along the lowest-energy migration pathways largely decide local barriers, intermediate trapping states and their structures, and thereby affect not only migration rates but also directional biases (both important for speed of advanced bipedal DNA motors, which typically use two ssDNA migrators as legs). This study thus provides a symmetry-based unified framework to analyze all possible inter-overhang ssDNA migrations, and guide their optimization in energetics, kinetics and structures for better DNA nanowalkers and many more dynamic DNA nanotechnological systems.

Conflicts of interest

There are no conflicts to declare.

Acknowledgements

This work was supported by Ministry of Education of Singapore under Grant No. A-0008378-00-00, A-8000628-00/01-00, and A-8000982-00-00 (to Z. S. Wang).

References

1 Z. Wang, R. Hou and I. Y. Loh, *Nanoscale*, 2019, **11**, 9240–9263.
2 A. J. Thubagere, W. Li, R. F. Johnson, Z. Chen, S. Doroudi, Y. L. Lee, G. Izatt, S. Wittman, N. Srinivas, D. Woods, *et al.*, *Science*, 2017, **357**, eaan6558.
3 J. Li, A. Johnson-Buck, Y. R. Yang, W. M. Shih, H. Yan and N. G. Walter, *Nat. Nanotechnol.*, 2018, **13**, 723–729.
4 J. Bath, S. J. Green and A. J. Turberfield, *Angew. Chem., Int. Ed.*, 2005, **44**, 4358–4361.
5 Y. Tian, Y. He, Y. Chen, P. Yin and C. Mao, *Angew. Chem.*, 2005, **117**, 4429–4432.
6 J. Cheng, S. Sreelatha, R. Hou, A. Efremov, R. Liu, J. R. van der Maarel and Z. Wang, *Phys. Rev. Lett.*, 2012, **109**, 238104.

7 I. Y. Loh, J. Cheng, S. R. Tee, A. Efremov and Z. Wang, *ACS Nano*, 2014, **8**, 10293–10304.
8 Y. Chiang, S. Tsai, S. Tee, O. Nair, I. Loh, M. Liu and Z. Wang, *Nanoscale*, 2018, **10**, 9199–9211.
9 M. Liu, J. Cheng, S. R. Tee, S. Sreelatha, I. Y. Loh and Z. Wang, *ACS Nano*, 2016, **10**, 5882–5890.
10 X. Hu, X. Zhao, I. Y. Loh, J. Yan and Z. Wang, *Nanoscale*, 2021, **13**, 13195–13207.
11 X. R. Liu, X. Hu, I. Y. Loh and Z. Wang, *Nanoscale*, 2022, **14**, 5899–5914.
12 M. You, Y. Chen, X. Zhang, H. Liu, R. Wang, K. Wang, K. R. Williams and W. Tan, *Angew. Chem., Int. Ed.*, 2012, **51**, 2457–2460.
13 T.-G. Cha, J. Pan, H. Chen, J. Salgado, X. Li, C. Mao and J. H. Choi, *Nat. Nanotechnol.*, 2014, **9**, 39–43.
14 K. Yehl, A. Mugler, S. Vivek, Y. Liu, Y. Zhang, M. Fan, E. R. Weeks and K. Salaita, *Nat. Nanotechnol.*, 2016, **11**, 184–190.
15 H. Peng, X.-F. Li, H. Zhang and X. C. Le, *Nat. Commun.*, 2017, **8**, 1–13.
16 K. Lund, A. J. Manzo, N. Dabby, N. Michelotti, A. Johnson-Buck, J. Nangreave, S. Taylor, R. Pei, M. N. Stojanovic, N. G. Walter, *et al.*, *Nature*, 2010, **465**, 206–210.
17 S. Piranej, A. Bazrafshan and K. Salaita, *Nat. Nanotechnol.*, 2022, **17**, 514–523.
18 Y. Gao, L. K. Wolf and R. M. Georgiadis, *Nucleic Acids Res.*, 2006, **34**, 3370–3377.
19 D. Y. Zhang and E. Winfree, *J. Am. Chem. Soc.*, 2009, **131**, 17303–17314.
20 S. A. Mortimer, M. A. Kidwell and J. A. Doudna, *Nat. Rev. Genet.*, 2014, **15**, 469–479.
21 W. F. Lima, B. P. Monia, D. J. Ecker and S. M. Freier, *Biochemistry*, 1992, **31**, 12055–12061.
22 T. E. Ouldridge, A. A. Louis and J. P. Doye, *J. Chem. Phys.*, 2011, **134**, 085101.
23 T. E. Ouldridge, *Coarse-grained modelling of DNA and DNA self-assembly*, Springer Science & Business Media, 2012.
24 T. E. Ouldridge, A. A. Louis and J. P. Doye, *Phys. Rev. Lett.*, 2010, **104**, 178101.
25 T. E. Ouldridge, P. Šulc, F. Romano, J. P. Doye and A. A. Louis, *Nucleic Acids Res.*, 2013, **41**, 8886–8895.
26 T. E. Ouldridge, R. L. Hoare, A. A. Louis, J. P. Doye, J. Bath and A. J. Turberfield, *ACS Nano*, 2013, **7**, 2479–2490.
27 Q. Yeo, I. Loh, S. Tee, Y. Chiang, J. Cheng, M. Liu and Z. Wang, *Nanoscale*, 2017, **9**, 12142–12149.
28 D. C. Khara, J. S. Schreck, T. E. Tomov, Y. Berger, T. E. Ouldridge, J. P. Doye and E. Nir, *Nucleic Acids Res.*, 2018, **46**, 1553–1561.
29 P. Šulc, T. E. Ouldridge, F. Romano, J. P. Doye and A. A. Louis, *Nat. Comput.*, 2014, **13**, 535–547.
30 S. Naskar and P. K. Maiti, *J. Mater. Chem. B*, 2021, **9**, 5102–5113.
31 B. E. Snodin, F. Randisi, M. Mosayebi, P. Šulc, J. S. Schreck, F. Romano, T. E. Ouldridge, R. Tsukanov, E. Nir, A. A. Louis, *et al.*, *J. Chem. Phys.*, 2015, **142**, 234901.
32 A. Sengar, T. E. Ouldridge, O. Henrich, L. Rovigatti and P. Šulc, *Front. Mol. Biosci.*, 2021, **8**, 693710.
33 A. Szabo, K. Schulten and Z. Schulten, *J. Chem. Phys.*, 1980, **72**, 4350–4357.
34 E. Poppleton, J. Bohlin, M. Matthies, S. Sharma, F. Zhang and P. Šulc, *Nucleic Acids Res.*, 2020, **48**, e72–e72.
35 S. Whitelam and P. L. Geissler, *J. Chem. Phys.*, 2007, **127**, 154101.
36 G. M. Torrie and J. P. Valleau, *J. Comput. Phys.*, 1977, **23**, 187–199.
37 E. Poppleton, R. Romero, A. Mallya, L. Rovigatti and P. Šulc, *Nucleic Acids Res.*, 2021, **49**, W491–W498.
38 N. Srinivas, T. E. Ouldridge, P. Šulc, J. M. Schaeffer, B. Yurke, A. A. Louis, J. P. Doye and E. Winfree, *Nucleic Acids Res.*, 2013, **41**, 10641–10658.
39 M. I. Wallace, L. Ying, S. Balasubramanian and D. Klenerman, *Proc. Natl. Acad. Sci. U. S. A.*, 2001, **98**, 5584–5589.
40 J. Fu, Y. R. Yang, A. Johnson-Buck, M. Liu, Y. Liu, N. G. Walter, N. W. Woodbury and H. Yan, *Nat. Nanotechnol.*, 2014, **9**, 531–536.
41 D. Fan, W. Zheng, R. Hou, F. Li and Z. Wang, *Biochemistry*, 2008, **47**, 4733–4742.
42 S. F. Wickham, M. Endo, Y. Katsuda, K. Hidaka, J. Bath, H. Sugiyama and A. J. Turberfield, *Nat. Nanotechnol.*, 2011, **6**, 166–169.
43 S. Winna, H. L. Too, A. Tommy, X. R. Liu, I. Y. Loh and Z. Wang, 2023. to be published.
44 K. Visscher, M. J. Schnitzer and S. M. Block, *Nature*, 1999, **400**, 184–189.
45 W. Zheng, D. Fan, M. Feng and Z. Wang, *Phys. Biol.*, 2009, **6**, 036002.
46 Z. Wang, *Proc. Natl. Acad. Sci. U. S. A.*, 2007, **104**, 17921–17926.
47 S. Rice, A. W. Lin, D. Safer, C. L. Hart, N. Naber, B. O. Carragher, S. M. Cain, E. Pechatnikova, E. M. Wilson-Kubalek, M. Whittaker, *et al.*, *Nature*, 1999, **402**, 778–784.
48 Y. Xu and Z. Wang, *J. Chem. Phys.*, 2009, **131**, 12B621.
49 J. Cheng, S. Sreelatha, I. Y. Loh, M. Liu and Z. Wang, *Methods*, 2014, **67**, 227–233.
50 M. Liu, R. Hou, J. Cheng, I. Y. Loh, S. Sreelatha, J. N. Tey, J. Wei and Z. Wang, *ACS Nano*, 2014, **8**, 1792–1803.
51 S. R. Tee, X. Hu, I. Y. Loh and Z. Wang, *Phys. Rev. Appl.*, 2018, **9**, 034025.
52 A. Efremov and Z. Wang, *Phys. Chem. Chem. Phys.*, 2011, **13**, 6223–6233.
53 A. Efremov and Z. Wang, *Phys. Chem. Chem. Phys.*, 2011, **13**, 5159–5170.
54 Z. Wang, R. Hou and A. Efremov, *J. Chem. Phys.*, 2013, **139**, 035105.